Optics Letters

Triaxially strained suspended graphene for large-area pseudo-magnetic fields

Manlin Luo,[1,†] Hao Sun,[2,†] Zhipeng Qi,[3] Kunze Lu,[1] Melvina Chen,[1] Dongho Kang,[1,4] Youngmin Kim,[1] Daniel Burt,[1] Xuechao Yu,[1] Chongwu Wang,[1] Young Duck Kim,[5] Hong Wang,[1] Qi Jie Wang,[1,2] and Donguk Nam[1,*]

[1]School of Electrical and Electronic Engineering, Nanyang Technological University, 50 Nanyang Avenue, Singapore 639798, Singapore
[2]Division of Physics and Applied Physics, School of Physical and Mathematical Sciences, Nanyang Technological University, 21 Nanyang Link, Singapore 637371, Singapore
[3]School of Physics and Optoelectronic Engineering, Nanjing University of Information Science & Technology, Nanjing 210044, China
[4]School of Electrical Engineering and Computer Science, Gwangju Institute of Science and Technology, Gwangju 61005, Republic of Korea
[5]Department of Physics, Kyung Hee University, Seoul 02447, Republic of Korea
*Corresponding author: dnam@ntu.edu.sg
†These authors contributed equally to this work.

Received 8 February 2022; revised 24 March 2022; accepted 26 March 2022; posted 28 March 2022; published 19 April 2022

Strain-engineered graphene has garnered much attention recently owing to the possibilities of creating substantial energy gaps enabled by pseudo-magnetic fields (PMFs). While theoretical works proposed the possibility of creating large-area PMFs by straining monolayer graphene along three crystallographic directions, clear experimental demonstration of such promising devices remains elusive. Herein, we experimentally demonstrate a triaxially strained suspended graphene structure that has the potential to possess large-scale and quasi-uniform PMFs. Our structure employs uniquely designed metal electrodes that function both as stressors and metal contacts for current injection. Raman characterization and tight-binding simulations suggest the possibility of achieving PMFs over a micrometer-scale area. Current–voltage measurements confirm an efficient current injection into graphene, showing the potential of our devices for a new class of optoelectronic applications. We also theoretically propose a photonic crystal-based laser structure that obtains strongly localized optical fields overlapping with the spatial area under uniform PMFs, thus presenting a practical route toward the realization of graphene lasers.

https://doi.org/10.1364/OL.455569

The discovery of graphene has created new opportunities in various distinct research fields, such as condensed matter physics and high-performance electronics and optoelectronics [1]. Despite its countless superior properties, graphene's gapless feature has been considered a major bottleneck toward creating bandgap-enabled nanoelectronic devices for switching applications [2] and nanophotonic devices possessing strong bandgap transitions [3]. Among a large variety of approaches for creating energy gaps [3–5], strain engineering has arisen as one of the strongest candidates for producing gapped graphene [5]. For instance, it was theoretically predicted that gapless graphene can have sizable energy gaps upon the application of more than 20% strain [5]. However, most works attempting to strain large-area monolayer graphene have reported limited strain values of less than 1.5% [6,7], thereby suppressing the hope of creating strain-induced energy gaps in graphene.

It is well known that charge carriers confined to two dimensions travel in cyclotron orbits under a strong magnetic field, resulting in the creation of energy gaps enabled by Landau quantization [8]. It was theoretically predicted that a well-designed strain in graphene can also allow the charge carriers to behave in the same way without requiring the use of an external magnetic field [9]. This effect was termed pseudo-magnetic fields (PMFs) [9].

Over the past decade, the existence of PMFs has been experimentally proven by scanning tunneling spectroscopy on deformed graphene sheets [10,11]. Very recently, it was demonstrated that the PMFs in such deformed monolayer graphene sheets can significantly influence the hot carrier dynamics by creating large pseudo-Landau levels [12]. Unfortunately, however, the spatial area of the induced PMFs in most studies reported until today is limited to the nanometer scale [10–12], which has prevented researchers from harnessing the unique PMFs in optoelectronic devices because of the micrometer-scale optical diffraction limit. A few research groups have recently reported the possibility of creating large-scale PMFs [13–16]. However, it remains elusive whether it is feasible to achieve spatially uniform PMFs at the micrometer scale, which holds the key toward harnessing PMFs for optoelectronic applications.

In this work, we present an experimental demonstration of triaxially strained suspended graphene that can obtain quasi-uniform PMFs over a large scale. The unique design of our structure allows achieving a micrometer-scale non-uniform strain with a relatively constant strain gradient, which plays an important role in obtaining uniform PMFs. We note that PMFs can also be generated by nanoscale confinement [4,17]. Since our structure is at the micrometer scale, nanoscale confinement is not a key factor in creating PMFs. Three arms of precisely

Corrected 18 July 2022

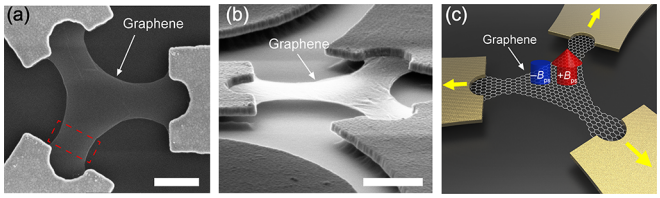

Fig. 1. (a), (b) SEM images showing fully suspended graphene contacted with metal pads. The graphene membranes are suspended about 200 nm above the SiO_2 layer. (a) Top view. Scale bar, 1 μm. (b) Tilted view. Scale bar, 1 μm. (c) Schematic of a typical triaxially strained graphene device deformed by three metal stressor pads, attaining a uniform PMF in the center.

patterned graphene are attached to three metal stressors, which also allow an efficient current injection into graphene. We also propose a hybrid laser structure employing a two-dimensional (2D) photonic crystal and triaxially strained graphene as an optical cavity and gain medium, respectively. Full three-dimensional (3D) finite-difference time-domain (FDTD) simulations confirm a strong optical mode overlap with an area under uniform PMFs. Our results suggest a new route to realize high-performance graphene optoelectronic devices by harnessing large-scale uniform PMFs in uniquely strained graphene.

Figures 1(a) and 1(b) show top- and tilted-view scanning electron microscopy (SEM) images of the fabricated device, where a fully suspended graphene sheet is attached to three metal pads. The device consists of four layers: the metal layer, chemical vapor deposition (CVD)-grown monolayer graphene, 300 nm thermally grown silicon dioxide (SiO_2), and a silicon (Si) wafer.

Highly stressed metals allow us to induce strain in a controllable way. The stress can be induced using two methods. One method is to use forming gas annealing. In this method, 10 nm chromium (Cr) and 140 nm gold (Au) were first deposited by electron beam evaporation and then subjected to forming gas annealing (300 °C, 30 min). The resultant strain is ~530 MPa, measured by laser scanning. By scanning the surface of a wafer before and after metal deposition, we can derive the curvature change of the wafer by calculating the displacement of the reflected beam [18].

Another way we applied to induce strain is using the internal stress of the Cr layer. In this method, four layers of metal consisting of 10 nm Cr, 70 nm Au, 40 nm Cr, and 70 nm Au are deposited sequentially. The resultant internal stress is ~500 MPa. The amount of strain can be easily controlled by modifying the thickness of the Cr between two Au layers [19,20]. It is desirable for the entire fabrication flow that the step of thermal annealing and the requirement for a vacuum furnace are eliminated. This strain-engineering method of harnessing internal stress in a film has been studied in other materials [21–27], but not in graphene.

The CVD graphene was patterned using electron beam lithography in a triaxial structure with three narrow neck regions (Fig. 1(a), dashed box). The grain size of the CVD monolayer graphene is around 80 μm, and we confirmed that the device size is within one grain boundary, thereby excluding any possibility of grain boundary-induced strain effects. Once the underlying SiO_2 is etched away, the released stressed metal film shrinks in size, stretching the patterned graphene sheet along three crystallographic directions, creating out-of-plane PMFs. Further fabrication details are described in the supplementary material. Figure 1(c) presents a schematic illustration of a typical

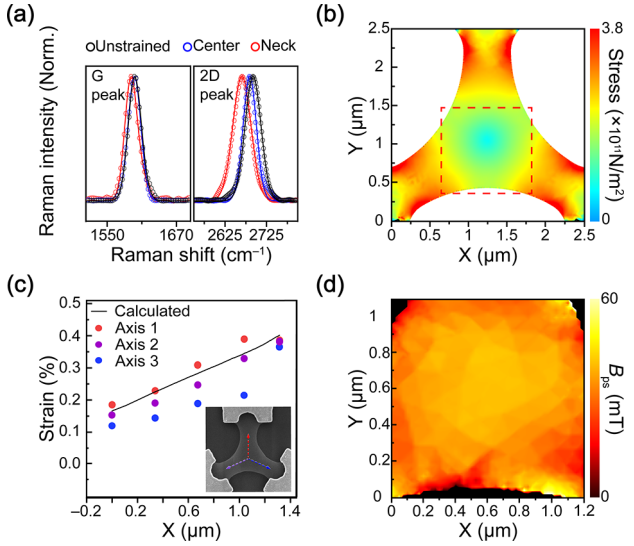

Fig. 2. (a) Raman spectra at the neck region and the center of a triaxially strained graphene device. Symbols are measurement data; curves are fitting data. (b) Simulated stress distribution in a graphene device calculated by the FEM simulation. (c) Experimentally determined line cut of 2D Raman peaks along three dashed arrows shown in the inset. The theoretically calculated result (solid line) is also presented for comparison. (d) Calculated PMF for the boxed region in (b).

triaxially strained graphene device configuration. The induced non-uniform strain creates PMFs [9,15,28], which are illustrated by the out-of-plane arrows. The time-reversal symmetry is preserved without the application of an external magnetic field, which gives rise to PMFs of opposite signs in the K and K′ valleys [10,11,29–32].

We conducted Raman scans to infer the strain using a 532 nm laser source. Figure 2(a) presents the Raman spectra measured for graphene at the center of the suspended membrane and at the most strained neck region, showing a clear strain-induced shift. The strain value can be derived by using a 2D peak strain-shift coefficient of –65.4 cm^{-1}/% [33]. The measured strain values for Raman spectra at the neck and the center regions of a triaxially strained graphene are 0.41 and 0.13%, respectively. It is found that the strain at the neck region decreases upon increasing the neck width, and there is a trade-off between the active area of the device and the amount of strain.

Figure 2(b) shows a simulated strain distribution performed by finite-element method (FEM) mechanical simulations. The experimental parameters of the device shown in Fig. 1(a) are used for the structural dimensions and residual stress in the metal pads. The simulated strain values for the center and the neck are 0.18 and 0.39%, respectively. Figure 2(c) compares the calculated (solid line) and experimentally measured (dots) one-dimensional (1D) strain distributions along three crystallographic directions. The three directions are highlighted as dotted lines in the inset. The calculated curve is in reasonable agreement with our experimentally measured strain values. The discrepancy between simulation and experimental results may be attributed to the unintentional doping in the CVD graphene layer [34], which may lead to a microscopic spatial variation in the measured Raman shift values. The strain distributions show a gradually increasing strain trend toward the neck region of the triaxial structure. As theoretically proposed by Guinea *et al.* [9],

this structure with a gradually changing strain distribution can induce uniform PMFs that lead to a large variety of new physical phenomena, including the zero-field quantum Hall effect [9] and pseudo-Landau level lasers [28].

Figure 2(d) presents a simulated spatial distribution of PMFs in our experimentally fabricated structure. The gauge potential, $\vec{A}$, is created by the in-plane strain in our structure and can be related to the strain tensors as in the following expression [9,28]:

$$\vec{A} = (A_x, A_y), \quad A_x = \frac{\beta}{2a_0}(\varepsilon_{xx} - \varepsilon_{yy}), \quad A_y = \frac{-\beta}{a_0}(\varepsilon_{xy}), \tag{1}$$

where β is a constant connecting hopping energy and bond lengths [35], a_0 is the bond length constant [28,35], and ε_{xx}, ε_{yy}, and ε_{xy} are the in-plane strain tensor elements [28,35]. The PMFs, B_{ps}, can also be calculated by using the following relation between the gauge potential and PMFs [9]:

$$B_{ps} = \partial_x A_y - \partial_y A_x. \tag{2}$$

More details on the calculation of PMFs can be found in Guinea *et al.* [9] and Sun *et al.* [28]. As shown in Fig. 2(d), the spatial distribution of PMFs can be uniform over a large scale with a maximum field strength of ~0.04 T.

The strength of PMFs is mainly determined by the intensity of the strain gradient, which is clearly evidenced by Eqs. (1) and (2). The strain gradient can be further increased by inducing a higher maximum strain in the neck region while keeping the size of the strained graphene structure. The maximum strain in the neck region can be conveniently tuned by changing the undercut length of the metal stressing pads, L_{metal}, which is defined in the supplementary Fig. S1.

To show the possibility of achieving stronger PMFs in our proposed structure, we performed further FEM simulations on the same triaxially strained structure for various values of the maximum strain in the neck region. Figure 3(a) shows the strength of the uniform PMF at the center of graphene as a function of strain in the neck region. The strength of PMFs reaches up to 2.9 T when the strain in the neck region is assumed to be 20%, which is an experimentally achieved level [36]. This unique ability of our structure to tune the strength of PMFs allows creating distinct graphene optoelectronic devices with different Landau-quantized energy gaps on a single die. Figure 3(b) displays the density of states curve) and 0.04 T (blue curve). The pseudo-Landau level peaks arise under the influence of PMFs, which could modify the optical response of graphene optoelectronic devices. The detailed calculation procedure of the density of states (DOS) is provided by Sun *et al.* [28]. Photoabsorption measurements can reveal the modified optical properties

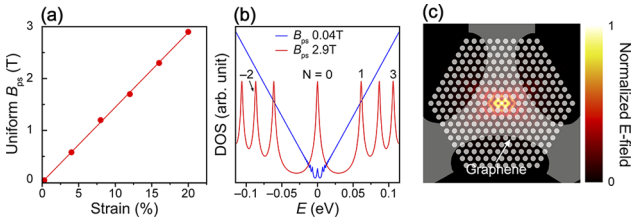

Fig. 3. (a) Intensity of the uniform PMF at the center as a function of the maximum strain in the graphene neck region. (b) Calculated DOS of graphene with a PMF intensity of 0.04 T and the largest PMF of 2.9 T shown in (a), where N is the index of the Landau level. (c) FDTD simulation of the PCC for the largest PMF shown in (a).

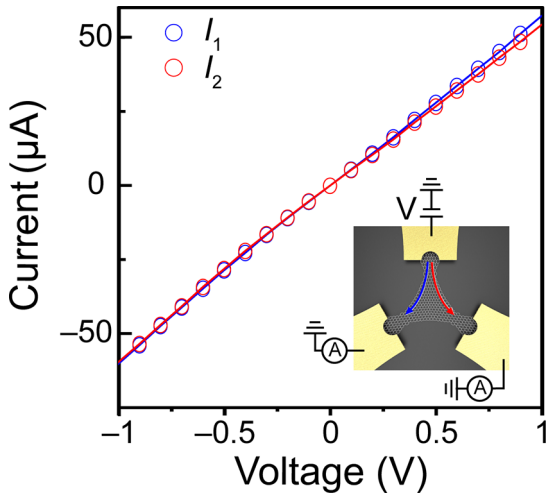

Fig. 4. Corresponding *I*–*V* curves measured at a zero back-gate voltage. The inset shows a schematic of our device with two experimentally measured current channels highlighted with left and right arrows.

in graphene with pseudo-Landau levels, which is the subject of further study. Previous studies on graphene under real magnetic fields proved the existence of Landau levels by showing enhanced absorption [37]. Our triaxially strained graphene can also be used to realize graphene Landau-level lasers [28,38].

Figure 3(c) displays a 3D FDTD simulation result showing a localized optical field at the center of a 2D photonic crystal cavity (PCC). The base structure is composed of a 3-μm-thick silicon slab with a lattice of holes. The hole radius and the periodicity are 2.1 μm and 6 μm, respectively. Triaxially strained graphene is also schematically drawn on top of the cavity. The central area of strained graphene possesses highly uniform PMFs, as shown in Fig. 2(d), and is spatially overlapped with the strong optical field. For a wavelength of 20.6 μm, a quality factor of ~10,000 can be realized according to the simulation. As proposed by Sun *et al.* [28], this highly practical structure can be used to achieve population inversion and significant optical net gain in graphene, thus allowing the realization of strained graphene Landau-level lasers. Our device can be further utilized to create circularly polarized lasers upon selectively exciting charge carriers only to a single valley, which can serve as a stepping stone for realizing polarization-division multiplexing in graphene-based photonic-integrated circuits [39].

The current–voltage (*I*–*V*) relation for suspended monolayer graphene at zero back-gate voltage is been plotted in Fig. 4. We apply a bias voltage between two of the three electrodes and form a current channel, giving rise to I_1 and I_2, which correspond to the currents along the left and right arrows, as illustrated in the inset. The similar *I*–*V* behavior of the two channels implies that all electrodes possess the same capacity to function as both stressors and metal contacts for current injection. It is worth noting that this triaxial platform could offer a new way to detect the valley Hall effect. Since the K- and K′-valley fermions are separated by PMFs, carriers located in opposite valleys could accumulate on different edges of the triaxial graphene membrane and move along two channels separately [11]. An imbalance between the K and K′ valleys can be experimentally imaged under the excitation of a circularly polarized light over a micrometer-scale central active region [40].

In conclusion, we have presented an experimental demonstration of triaxially strained suspended graphene structures. Our unique design may allow obtaining large-area, uniform PMFs, which can play major roles in harnessing PMFs for a new class of graphene-based optoelectronic devices. Our device can be utilized to realize practical valleytronic devices, including valleytronic transistors [41] and valley filters [11,42]. In addition, the ability to tune the strength of PMFs via conventional lithography should enable the creation of distinct graphene optoelectronic devices with different Landau-quantized energy gaps on a single die. The presented structure is expected to be very general and can be employed to induce customized strain in any 2D material. We believe that our device lays the groundwork for bringing the performance of graphene-based optoelectronics to another level.

Funding. iGrant of Singapore (A*STAR AME IRG (A2083c0053)); National Research Foundation Singapore (Competitive Research Program (NRF-CRP19-2017-01), NRF-ANR Joint Grant (NRF2018-NRF-ANR009 TIGER)); Ministry of Education - Singapore (AcRF TIER (RG 115/21), AcRF TIER 2 (MOE2018-T2-2-011 (S))).

Acknowledgment. The authors gratefully thank M. M. Deshmukh for the insightful discussions.

Disclosures. The authors declare no competing interests.

Data availability. Data underlying the results presented in this paper are not publicly available at this time but may be obtained from the authors upon reasonable request.

Supplemental document. See Supplement 1 for supporting content.

REFERENCES

1. F. Bonaccorso, Z. Sun, T. Hasan, and A. C. Ferrari, Nat. Photonics **4**, 611 (2010).
2. N. O. Weiss, H. Zhou, L. Liao, Y. Liu, S. Jiang, Y. Huang, and X. Duan, Adv. Mater. **24**, 5782 (2012).
3. Y. Zhang, T. T. Tang, C. Girit, Z. Hao, M. C. Martin, A. Zettl, M. F. Crommie, Y. R. Shen, and F. Wang, Nature **459**, 820 (2009).
4. L. A. Ponomarenko, F. Schedin, M. I. Katsnelson, R. Yang, E. W. Hill, K. S. Novoselov, and A. K. Geim, Science **320**, 356 (2008).
5. C. Si, Z. Sun, and F. Liu, Nanoscale **8**, 3207 (2016).
6. T. M. G. Mohiuddin, A. Lombardo, R. R. Nair, A. Bonetti, G. Savini, R. Jalil, N. Bonini, D. M. Basko, C. Galiotis, N. Marzari, K. S. Novoselov, A. K. Geim, and A. C. Ferrari, Phys. Rev. B **79**, 205433 (2009).
7. X. Gao, H. Sun, D. H. Kang, C. Wang, Q. J. Wang, and D. Nam, Sci. Rep. **11**, 1 (2021).
8. P. Plochocka, P. Kossacki, A. Golnik, T. Kazimierczuk, C. Berger, W. A. De Heer, and M. Potemski, Phys. Rev. B **80**, 245415 (2009).
9. F. Guinea, M. I. Katsnelson, and A. K. Geim, Nat. Phys. **6**, 30 (2010).
10. N. Levy, S. A. Burke, K. L. Meaker, M. Panlasigui, A. Zettl, F. Guinea, A. H. Castro Neto, and M. F. Crommie, Science **329**, 544 (2010).
11. C. C. Hsu, M. L. Teague, J. Q. Wang, and N. C. Yeh, Sci. Adv. **6**, 1 (2020).
12. D. H. Kang, H. Sun, M. Luo, K. Lu, M. Chen, Y. Kim, Y. Jung, X. Gao, S. J. Parluhutan, J. Ge, S. W. Koh, D. Giovanni, T. C. Sum, Q. J. Wang, H. Li, and D. Nam, Nat. Commun. **12**, 1 (2021).
13. Y. Liu, J. N. B. Rodrigues, Y. Z. Luo, L. Li, A. Carvalho, M. Yang, E. Laksono, J. Lu, Y. Bao, H. Xu, S. J. R. Tan, Z. Qiu, C. H. Sow, Y. P. Feng, A. H. C. Neto, S. Adam, J. Lu, and K. P. Loh, Nat. Nanotechnol. **13**, 828 (2018).
14. C. S. C. Downs, A. Usher, and J. Martin, J. Appl. Phys. **119**, 194305 (2016).
15. G. J. Verbiest, S. Brinker, and C. Stampfer, Phys. Rev. B **92**, 075417 (2015).
16. H. Shi, Z. Zhan, Z. Qi, K. Huang, E. van Veen, JÁ Silva-Guillén, R. Zhang, P. Li, K. Xie, H. Ji, M. I. Katsnelson, S. Yuan, S. Qin, and Z. Zhang, Nat. Commun. **11**, 1 (2020).
17. H. C. Chung, C. P. Chang, C. Y. Lin, and M. F. Lin, Phys. Chem. Chem. Phys. **18**, 7573 (2016).
18. B. Kebabi, C. K. Malek, and F. R. Ladan, Vacuum **41**, 1353 (1990).
19. R. Abermann, Vacuum **41**, 1279 (1990).
20. J. Kim, H. Park, J. B. Hannon, S. W. Bedell, K. Fogel, D. K. Sadana, and C. Dimitrakopoulos, Science **342**, 833 (2013).
21. S. Bao, D. Kim, C. Onwukaeme, S. Gupta, K. Saraswat, K. H. Lee, Y. Kim, D. Min, Y. Jung, H. Qiu, H. Wang, E. A. Fitzgerald, C. S. Tan, and D. Nam, Nat. Commun. **8**, 1 (2017).
22. D. Nam, D. S. Sukhdeo, J. H. Kang, J. Petykiewicz, J. H. Lee, W. S. Jung, J. Vučković, M. L. Brongersma, and K. C. Saraswat, Nano Lett. **13**, 3118 (2013).
23. J. Petykiewicz, D. Nam, D. S. Sukhdeo, S. Gupta, S. Buckley, A. Y. Piggott, J. Vučković, and K. C. Saraswat, Nano Lett. **16**, 2168 (2016).
24. Z. Qi, H. Sun, M. Luo, Y. Jung, and D. Nam, J. Phys.: Condens. Matter **30**, 334004 (2018).
25. D. Nam, D. Sukhdeo, A. Roy, K. Balram, S.-L. Cheng, K. C.-Y. Huang, Z. Yuan, M. Brongersma, Y. Nishi, D. Miller, and K. Saraswat, Opt. Express **19**, 25866 (2011).
26. Y. Jung, Y. Kim, D. Burt, H.-J. Joo, D.-H. Kang, M. Luo, M. Chen, L. Zhang, C. S. Tan, and D. Nam, Opt. Express **29**, 14174 (2021).
27. D. S. Sukhdeo, D. Nam, J.-H. Kang, M. L. Brongersma, and K. C. Saraswat, Photonics Res. **2**, A8 (2014).
28. H. Sun, Z. Qi, Y. Kim, M. Luo, B. Yang, and D. Nam, Opt. Express **29**, 1892 (2021).
29. S. Zhu, J. A. Stroscio, and T. Li, Phys. Rev. Lett. **115**, 245501 (2015).
30. Y. Jiang, J. Mao, J. Duan, X. Lai, K. Watanabe, T. Taniguchi, and E. Y. Andrei, Nano Lett. **17**, 2839 (2017).
31. X. P. Zhang, C. Huang, and M. A. Cazalilla, 2D Mater. **4**, 024007 (2017).
32. M. Settnes, S. R. Power, and A. P. Jauho, Phys. Rev. B **93**, 035456 (2016).
33. M. A. Bissett, W. Izumida, R. Saito, and H. Ago, ACS Nano **6**, 10229 (2012).
34. E. Cazalas, I. Childres, A. Majcher, T. F. Chung, Y. P. Chen, and I. Jovanovic, Appl. Phys. Lett. **103**, 053123 (2013).
35. V. M. Pereira, A. H. C. Neto, and N. M. R. Peres, Phys. Rev. B **80**, 045401 (2009).
36. C. Lee, X. Wei, J. W. Kysar, and J. Hone, Science **321**, 385 (2008).
37. M. L. Sadowski, G. Martinez, M. Potemski, C. Berger, and W. A. De Heer, Phys. Rev. Lett. **97**, 266405 (2006).
38. F. Wendler and E. Malic, Sci. Rep. **5**, 12646 (2015).
39. J. T. Kim, J. H. Choe, J. S. Kim, D. Seo, Y. D. Kim, and K. H. Chung, Opt. Laser Technol. **106**, 76 (2018).
40. K. F. Mak, D. Xiao, and J. Shan, Nat. Photonics **12**, 451 (2018).
41. L. Li, L. Shao, X. Liu, A. Gao, H. Wang, B. Zheng, G. Hou, K. Shehzad, L. Yu, F. Miao, Y. Shi, Y. Xu, and X. Wang, Nat. Nanotechnol. **15**, 743 (2020).
42. M. Settnes, S. R. Power, M. Brandbyge, and A. P. Jauho, Phys. Rev. Lett. **117**, 276801 (2016).